PASJ: Publ. Astron. Soc. Japan , 1–??,

Multiple Component Analysis of Time Resolved Spectra of GRB041006: A Clue to the Nature of Underlying Soft Component of GRBs.

Yuji Shirasaki, [1] Atsumasa Yoshida, [2,4] Nobuyuki Kawai, [3,4] Toru Tamagawa, [4] Takanori Sakamoto, [5] Motoko Suzuki, [6] Yujin Nakagawa, [2] Akina Kobayashi, [2] Satoshi Sugita, [2,4] Ichiro Takahashi, [2] Makoto Arimoto, [3] Takashi Shimokawabe [3] Nicolas Vasquez Pazmino, [3] Takuto Ishimura, [3] Rie Sato, [7] Masaru Matsuoka, [6] Edward E. Fenimore, [8] Mark Galassi, [8] Donald Q. Lamb, [9] Carlo Graziani, [9] Timothy Q. Donaghy, [9] Jean-Luc Atteia, [10] Alexandre Pelangeon, [10] Roland Vanderspek, [11] Geoffrey B. Crew, [11] John P. Doty, [11] Joel Villasenor, [11] Gregory Prigozhin, [11] Nat Butler, [11,12] George R. Ricker, [11] Kevin Hurley, [12] Stanford E. Woosley, [13] and Graziella Pizzichini [14]

[1] *National Astronomical Observatory of Japan, Osawa, Mitaka, Tokyo, 181-8588*
yuji.shirasaki@nao.ac.jp

[2] *Department of Physics and Mathematics, Aoyama Gakuin University, 5-10-1 Fuchinobe, Sagamihara, Kanagawa 229-8558*

[3] *Department of Physics, Tokyo Institute of Technology, 2-12-1 Ookayama, Meguro-ku, Tokyo 152-8551*

[4] *RIKEN, 2-1 Hirosawa, Wako Saitama 351-0198*

[5] *Goddard Space Flight Center, NASA, Greenbelt, Maryland, 20771, USA*

[6] *JAXA, 2-1-1 Sengen, Tsukuba, Ibaraki, 305-8505*

[7] *JAXA/ISAS, 3-1-1 Yoshinodai, Sagamihara, Kanagawa, 229-8510*

[8] *Los Alamos National Laboratory, P. O. Box 1663, Los Alamos, NM, 87545, USA*

[9] *Department of Astronomy and Astrophysics, University of Chicago, 5640 South Ellis Avenue, Chicago, Illinois 60637, USA*

[10] *LATT, Université de Toulouse, CNRS, 14 avenue E. Belin, 31400 Toulouse, France*

[11] *Center for Space Research, MIT, 77 Vassar Street, Cambridge, Massachusetts, 02139-4307, USA*

[12] *Space Sciences Laboratory, 7 Gauss Way, University of California , Berkeley, California, 94720-7450*

[13] *Department of Astronomy and Astrophysics, University of California at Sata Cruz, 477 Clark Kerr Hall, Santa Cruz, California, 95064, USA*

[14] *INAF/IASF Bologna, Via Gobetti 101, 40129 Bologna, Italy*

(Received 2008 February 12; accepted 2008 0)

Abstract

GRB 041006 was detected by HETE-2 at 12:18:08 UT on 06 October 2004. This GRB displays a soft X-ray emission, a precursor before the onset of the main event, and also a soft X-ray tail after the end of the main peak. The light curves in four different energy bands display different features; At higher energy bands several peaks are seen in the light curve, while at lower energy bands a single broader bump dominates. It is expected that these different features are the result of a mixture of several components each of which has different energetics and variability. To reveal the nature of each component, we analysed the time resolved spectra and they are successfully resolved into several components. We also found that these components can be classified into two distinct classes; One is a component which has an exponential decay of E_p with a characteristic timescale shorter than ~ 30 sec, and its spectrum is well represented by a broken power law function, which is frequently observed in many prompt GRB emissions, so it should have an internal-shock origin. Another is a component whose E_p is almost unchanged with characteristic timescale longer than ~ 60 sec, and shows a very soft emission and slower variability. The spectrum of the soft component is characterized by either a broken power law or a black body spectrum. This component might originate from a relatively wider and lower velocity jet or a photosphere of the fireball. By assuming that the soft component is a thermal emission, the radiation radius is initially 4.4×10^6 km, which is a typical radius of a blue supergiant, and its expansion velocity is 2.4×10^5 km/s in the source frame.

Key words: gamma-rays:busts — X-rays: bursts — X-rays: individual (GRB041006)

1. Introduction

On October 6, 2004 the High Energy Transient Explorer 2 (HETE-2) detected a gamma-ray burst (GRB) with soft X-ray emission before the onset of the main event. Such soft emission, a precursor, is predicted in some of theoretical models. The fireball undergoes a transition from an optically thick phase to an optically thin phase, and thermal radiation (the fireball precursor) may occur during this transition (B. Paczynsky 1986; Daigne

& Mochkovitch 2002). A precursor (progenitor precursor) may also be emitted by the interaction of the jet with the progenitor star (Ramirez-Ruiz et al. 2002; Waxman & Meszaros 2003). The external shock by the first relativistic shell can also produce the non-thermal precursor (Umeda et al. 2005).

Soft precursors are occasionally detected in long GRBs. The first detection was made by the GINGA satellite (GRB 900126; Murakami et al. 1991). In more recent observations, the BeppoSAX (e.g. GRB 011121; Piro et al. 2005), HETE2 (e.g. GRB 030329; Vanderspek et al. 2004) and Swift (e.g GRB 050820A; Cenko et al. 2006, GRB 060124; Romano et al. 2006, GRB 061121; Page et al. 2007) satellites have also detected precursors. Lazzati 2005 studied bright long BATSE GRB light curves and found that in 20% of the cases there is evidence for soft emission before the main event.

The precursor is usually detected as a single pulse that is well separated in time from the main event, typically several seconds to hundreds of seconds. The precursor of GRB 041006 is not well separated from the main event and is likely to be continuously active during the whole prompt GRB phase. Such a long lasting soft component was also observed in GRB 030329 (Vanderspek et al. 2004). Vetere et al. 2006 found that for some of the GRBs detected by the BeppoSAX, there is a slowly varying soft component underlying the highly variable main event. Borgonovo et al. 2007 analyzed the light curves obtained by BATSE, Konus, and BeppoSAX, and found that the width of the auto-correlation function shows a remarkable bimodal distribution in the rest-frame of the source. This result suggests that there exists a slowly varying soft component in some GRBs. The relation between the underlying soft X-ray component, the X-ray precursor, and the main event is still open to question.

In this paper, we present the results of multiple component analysis of the time resolved spectra of GRB 041006. Throughout this paper the peak energies are in the observaer's frame, and quoted errors are at 90% C.L., unless specified otherwise.

2. Observation

GRB 041006 was detected with the HETE FREGATE (Atteia et al. 2003) and the WXM (Shirasaki et al. 2003) instruments at 12:18:08 UT on 06 October 2004 (Galassi et al. 2004). The WXM flight software localized the burst in real time, resulting in a GCN Notice 42 seconds after the burst trigger. The prompt error region was a circle of 14 arcminute radius (90% confidence) centered at RA = 00h 54m 54s, DEC = +01d 18' 37" (J2000). Ground analyses of the burst data allowed the error region to be refined to a circle of 5.0 arcminute radius (90% confidence) centered at RA = 00h 54m 53s, DEC = +01d 12' 04" (J2000).

1.4 hours after the trigger, the optical afterglow was found by Da Costa et al. 2004, and the redshift was first reported by Fugazza et al. 2004 and later confirmed by Price et al. 2004 to be $z = 0.716$. Follow-up observations were made at various observation sites (e.g. Urata et al. 2007). VLA observations were made but no radio sources were detected (Soderberg et al. 2004). The X-ray afterglow was found by Butler et al. 2005, and it exhibited a power law decay with a slope of -1.0 ± 0.1. The X-ray spectrum was characterized by an absorbed power law model with a photon index of $\Gamma = 1.9 \pm 0.2$ and $n_H = (1.1 \pm 0.5) \times 10^{21}$ cm^{-2}. The emergence of a supernova component was reported by Bikmaev et al. 2004 and Garg et al. 2004. The field of GRB 041006 was imaged by Soderberg et al. 2006 using the WFC of the ACS on-board HST, and they found a SN 1998bw-like supernova dimmed by $\sim$0.3 magnitudes.

3. Analysis

The data obtained by the WXM and FREGATE instruments were reduced and calibrated in the standard manner. We used WXM TAG data and FREGATE PH data.

3.1. Temporal Properties

Figure 1 shows the light curves of GRB 041006 in four energy bands with 0.5 sec time resolution. T_{50} and T_{90} are measured for each energy band, and they are shown in Table 1.

The burst can be divided into four major intervals according to spectral features, and each major interval is divided into a few sub-intervals for time-resolved spectral analysis. The time intervals for each sub-interval are shown in Table 2. In interval 1 soft emission showing no prominent activity above 40 keV occurs, then harder emissions follow in intervals 2 and 3. In interval 4, the hard emission almost disappears and only gradually decaying soft emission is present.

We call the emission seen in interval 1 an X-ray precursor. The precursor shows a structured light curve in the lowest energy band (2$\sim$10 keV), which indicates that two emissions are occurring successively . In interval 2, two peaks are seen in the higher energy bands ($>$ 40 keV). The time history of the hardness ratio also clearly shows the corresponding peaks. In the lowest energy bands ($<$ 10 keV), structured emission is not clearly seen. In interval 3, two harder peaks are seen in the highest energy band ($80 \sim 400$ keV), and this structure is less distinct in the lower energy bands. The emission in interval 4, which we call an X-ray tail, shows no prominent structure.

From the dissimilarity of the light curves in the four energy bands, it is inferred that the total emission is composed of several independent emissions which have different characteristic energies. For an example, two components which contribute to the precursor, four components seen as a peak in the energy bands $40 \sim 80$ keV and $80 \sim 400$ keV, and one broad soft component which constitutes the major part of the light curve in the lowest energy band. To investigate this hypothesis, we performed time resolved spectral analysis based on a multiple-component spectrum model.

3.2. Average Spectral Properties

The joint spectral analysis of WXM and FREGATE data was performed using XSPEC v.11.3.1 (Arnaud 1996). The time integrated spectrum of GRB 041006 is approximately described by a broken power law function (Figure 2); the low energy photon index is $\alpha = 1.28 \pm 0.02$, the high energy index is $\beta = 2.14 \pm 0.07$, the break energy is $E_p = 22.5 \pm 1.7$ keV and the flux at 1 keV is $K = 4.25 \pm 0.15$ cm^{-2}s^{-1} keV^{-1}, where the quoted errors are one sigma. The χ^2 is 111.19 for 79 dof, and Null hypothesis probability is 0.0099, so the fit is not very good. From this fitting result, we obtained $S_X = (5.24 \pm 0.08) \times 10^{-6}$ ergs cm^{-2}, $S_\gamma = (7.13 \pm 0.12) \times 10^{-6}$ ergs cm^{-2}, where S_X and S_γ denote fluences in the 2$\sim$30 keV and 30$\sim$400 keV energy ranges and the error is 1 sigma. As the ratio of fluences is $\log(S_x/S_\gamma) = -0.13$, the GRB can be classified as an X-ray Rich GRB (Sakamoto et al. 2005).

The isotropic energy is calculated from:

$$E_{\rm iso} = \frac{4\pi D_L^2}{z+1} \int_{1/(z+1)}^{10^4/(z+1)} E\Phi dE \qquad (1)$$

where D_L is the luminosity distance, and Φ is the differential photon spectrum. We obtained $E_{\rm iso} = 2.54^{+0.46}_{-0.35} \times 10^{52}$ ergs. In Figure 3, the peak energy in the source frame $E_{\rm p,src}$ is plotted against the isotropic energy $E_{\rm iso}$ (the point labeled "Total"). The relation for GRB 041006 obtained from the one component fit is completely outside the Amati relation (Amati 2006).

Looking at the residual plot in the top panel of Figure 2, an additional soft component is apparently seen around 6 keV and a systematic excess is also seen around 50$\sim$100 keV. Thus the total spectrum was fitted by a superposition of multiple basic functions. As basic functions, we considered a broken power law and a black-body.

For the broken power law model, we used the following function to estimate the peak energy flux directly:

$$\begin{aligned} A(E) = K/E_p^2 (E/E_p)^{-\alpha}, \qquad & E \le E_p \\ K/E_p^2 (E/E_p)^{-\beta}, \qquad & E > E_p \end{aligned} \qquad (2)$$

The parameters α and β, which are the lower and higher energy photon indices, are restricted to the range of -2.0 $\sim$ 2.0 and 2.5 $\sim$ 5.0, respectively. The initial value of the break energy E_p of the `bknp` basic function is determined from the local excess of the residual between the single `bknp` model and the observed data. The restriction to the break energy E_p is applied so that the parameter converges around the initial value.

The results of the spectral fit for three three-component models are shown in Table 3. For comparison the result of the two-component model and a fit by the Band function (Band et al. 1993) and a broken power law function are also shown in the table. The fitting parameters for the models `bbody*2+bknp` and `bknp*3` are given in Table 4.

Akaike's Information Criterion (AIC) is calculated for each model. AIC (Akaike 1974) is a very widely used criterion to evaluate the goodness of the statistical model from both the goodness of fit and the complexity of the model. AIC is defined by the following equation:

$$AIC = n \ln\left(\frac{\chi^2}{n}\right) + 2k, \qquad (3)$$

where n is the number of data points, k is the number of free parameters to be estimated, and χ^2 is the residual sum of squares from the estimated model. The AIC includes a penalty that is an increasing function of the number of estimated parameters; overfitting is discouraged, and thus this method enables one to find the best model for the data, with minimum of free parameters. The model with the lower value of AIC is the one to be preferred.

The most preferable model is `bbody*2+bknp`. The model name is given by an algebraic expression of the name of a basic model. The second most preferable model is `bknp*3`. The AIC values for the two models are 6.87 and 8.47 respectively.

The lowest AIC does not necessarily select the true model, and the degree of the preference is estimated by the AIC difference. The relation between the degree of the preference and the AIC difference (Δ_X), however, depends on n and the models to be compared. So we evaluate the confidence limit of the AIC difference by carrying out a Monte Carlo simulation. The Monte Carlo simulation was performed by using the `fakeit` command of XSPEC, which generated 1000 PHA samples based on the spectral model to be tested. For each PHA sample, a spectral fit was performed for both the tested model and the model which gave the lowest AIC, and the AIC difference was calculated.

The left panel of Figure 4 shows a simulated distribution of the AIC difference $\Delta_{\texttt{bknp*3}} = {\rm AIC}_{\texttt{bknp*3}} - {\rm AIC}_{\texttt{bbody*2+bknp}}$. The simulation was performed with the model spectrum `bknp*3`; the model parameters were obtained from the fit to the observed total spectrum. For each simulated PHA sample, model fit was performed for both the `bknp*3` model and `bbody*2+bknp`, which is the most preferred model. From this result the 90% confidence limit for $\Delta_{\texttt{bknp*3}}$ is estimated as 4.7, below which 90% of samples are included. The observed AIC difference for the model `bknp*3` is 2.64, so the model is acceptable at 90% C.L. In the case of the Band model (right hand panel of Figure 4), for 98% of the samples the AIC is smaller than the most preferred model `bbody*2+bknp`. The observed AIC difference is 13.68, so the Band model is rejected at higher than 98% C.L. All the three three-component models are acceptable at 90% C.L. The two-component model is rejected at 90% C.L.

As the time averaged spectrum of GRB 041006 is well represented by a superposition of the three components, we examined the $E_{\rm p,src}$-$E_{\rm iso}$ relation for each one. The $E_{\rm iso}$ calculated for a model `bknp*3` are $1.36^{+0.4}_{-0.8} \times 10^{52}$ erg for $E_{\rm p,src} = 123^{+28}_{-17}$ keV, $0.28^{+1.0}_{-0.1} \times 10^{52}$ erg for $E_{\rm p,src} = 44^{+3.4}_{-6.9}$, and $0.94^{+1.6}_{-0.6} \times 10^{51}$ erg for $E_{\rm p,src} = 8.4^{+2.2}_{-1.0}$. The $E_{\rm iso}$ calculated for a model `bbody*2+bknp` is $1.32^{+0.47}_{0.25} \times 10^{52}$ erg for the high energy component with $E_p = 73.4 \pm 15$. The result are compared with the other

GRBs in Figure 3. The components with $E_p > 40$ keV and $E_p \sim 20$ keV are well within the Amati relation, and the component $E_p \sim$6 keV is out of the 90% distribution width of the Amati relation. The $\log(S_x/S_\gamma)$ for the three components are -0.3 for the component $E_p >$40 keV, 0.78 for the component $E_p \sim$20 keV, and 0.76 for the component $E_p \sim$6 keV; thus they are classified as XRR, XRF and XRF, respectively.

3.3. Time Resolved Spectral Properties

Time resolved spectral analysis was performed for 12 independent time intervals, and also for some intermediate intervals which overlap part of one or two adjacent intervals to trace the spectral evolution more closely. We applied multi-component models in the spectral fit, where the model spectrum is represented as a superposition of an arbitrary number of basic functions. The basic functions considered here are black body (`bbody`), broken power law (`bknp`), and a single power law function (`pl`). The XSPEC built-in model is used for `bbody` and `pl`, for which the XSPEC model names are `bbodyrad` and `powerlaw` respectively. For the broken power law model, we used Eq. 3.

The fitting results for various combinations of basic functions are summarized in Table 5. The fitting parameters for the lowest AIC model are shown in Table 6. The model spectra giving the lowest AIC at each interval are shown in Figures 6 and 7. The expected number of components constituting the total spectrum is inferred from the number of local excesses in the residual plot for the `bknp` model, and also from the light curves in the four energy bands. As an example, the case of interval 2c is shown in Figure 5. The spectrum is fitted with a single broken power law function, and E_p is determined as $\sim$20 keV. Looking at the residual plot shown in the bottom of the figure, local excesses around 6 keV and 60 keV are seen. So the spectrum of interval 2c is expected to be constituted from three components which have peak energies of 6, 20, and 60 keV. In the case of interval 2b at least four components are expected from the light curves. One is the precursor component seen in interval 1, which is expected to be present in interval 2 if it is extrapolated smoothly. Two components corresponding to the two peaks seen in the 40$\sim$80 keV energy band and one component corresponding to the broad soft emission in the lowest energy band are also expected to be present. So up to four components are examined for interval 2b.

The model selection is carried out by examining the AIC difference, and the 90% confidence limit of the AIC difference is calculated by performing a Monte Carlo simulation. By this statistical examination, single component models considered here are rejected for most of the intervals. The single component model is accepted only for intervals 1a, 4a, and 4b. For the other intervals, the single component model considered here is rejected at 90% C.L. and the multi-component models are preferred.

For most of the intervals, the null hypothesis probability is larger than 0.1. For interval 2b, however, the null hypothesis probability is at most 0.003. This is probably because unknown systematic errors are present in the data.

4. Discussion

The optical afterglow light curve in the R band can be fitted by a broken power-law model with a break time $t_b = 0.16 \pm 0.04$ days (Stanek et al. 2005). Taking t_b as a jet break time and assuming a homogeneous density profile around the GRB, the jet opening angle θ is estimated from the following equation (Sari et al. 1999, Nava et al. 2006):

$$\theta = 0.161 \left(\frac{t_b}{1+z}\right)^{3/8} \left(\frac{n_0 \eta_\gamma}{E_{\rm iso,52}}\right)^{1/8}, \quad (4)$$

where n_0 is the ambient particle density in cm^{-3}, η_γ the radiation efficiency, and $E_{\rm iso,52} = E_{\rm iso}/$ (10^{52} erg). Assuming $n_0 = 3$ and $\eta_\gamma = 0.2$, we obtain a jet opening angle of 3.4°. If the GRB is viewed on-axis, the collimation-corrected total energy can be estimated from $E_\gamma = (1 - \cos\theta) E_{\rm iso}$. The corrected total energies for the three components are $2.4^{+0.70}_{-1.4} \times 10^{49}$ erg for $E_{\rm p,src} = 123^{+28}_{-17}$ keV, $0.49^{+1.8}_{-0.2} \times 10^{49}$ erg for $E_{\rm p,src} = 44^{+3.4}_{-6.9}$, and $1.7^{+2.8}_{-1.1} \times 10^{48}$ erg for $E_{\rm p,src} = 8.4^{+2.2}_{-1.0}$. These values do not follow the Ghirlanda et al. 2007 relation except for the component with $E_p \sim 6$ keV. That is, the $E_{\rm p,src}$ expected from the Ghirlanda relation are 39.4, 13.0 and 6.2 keV for the components with $E_p >$ 40 keV, $\sim$ 20 keV, and $\sim$ 6 keV, respectively. Taking a 5% uncertainty in the Ghirlanda relation, the observed E_p for the the components with $E_p >$ 40 keV and $\sim$ 20 keV are incompatible.

Granot et al. 2005 showed that the afterglow light curve of GRB 041006 is naturally reproduced by an off-axis jet model, and that an on-axis model is hard to reconcile with the flat light curve observed at an early stage. If this is the case, the discrepancy with the Ghirlanda relation could be explained by the fact that the calculated E_γ is underestimated.

Looking at the time evolution of E_p obtained by the time resolved spectral analysis shown in Figure 8, we can identify seven components. Each component is interpolated with a solid line, and is given an identifier A, B_1, B_2, C_1, C_2, C_3 or C_4.

The most preferred spectral model for component A in interval 1a is the `bbody` model. The calculated emission radius is $4.35^{+1.4}_{-1.1} \times 10^6$ km, which corresponds to 6 solar radii and is a typical radius for a blue supergiant. The AIC difference for the second-most preferred `bknp` model is 3.31 and its 90% confidence limit is 4.9, so the `bknp` is also acceptable. The AIC differences for the power law spectrum with and without absorption (`wabs*pl` and `pl`) are larger than 8.9, and their 90% confidence limits are less than 0.3, so these models are rejected at 90% C.L.

For interval 1b, the acceptable models are `bbody*2`, `bbody+bknp` and `bknp*2`, all of which are two-component models. None of the single component models considered here is preferable and all are rejected at 90% C.L. Thus it is likely that the emission in interval 1b is composed of two components (A and B_1). The spectral type of each component is not uniquely determined from this result;

it is either a black body or a broken power law function. Assuming that component B_1 is black body radiation, the calculated emission radius is about one solar radius.

In intervals 2a $\sim$ 2d, the soft components A and B_1 are present in all the acceptable models. The peak energies of the components are almost constant during intervals 1 and 2, and they decrease slowly, with decay time 72 ± 42 sec for component A and 57 ± 33 sec for component B_1. Assuming that the components originate from thermal emission, we can derive the evolution of the radiation radii, and they are shown in Figure 9 with the filled circles for component A and with open circles for component B_1. The data points for component B_1 are shifted by a factor of four. The data points for intervals 1 and 2 are fitted with a linear function, and we calculate the apparent expansion velocity for component A to be $(6.3 \pm 1.5) \times 10^5$ km/s, which is twice the speed of light. This superluminal motion is observed when the emitter is moving with relativistic velocity toward the observer. The relation between the apparent expansion velocity v and the velocity measured in the source frame v' is given by:

$$v = \frac{v'}{(1+z)(1-\frac{v'}{c})}. \quad (5)$$

The expansion velocity in the source frame is 2.35×10^5 km/s, and the corresponding Lorenz factor is 1.6. The apparent expansion rate for component B_1 is found to be 1.1×10^5 km/s, and the velocity in the source frame is 1.2×10^5 km/s, which is half the velocity of component A.

If the component originates in an internal shock according to the model of Zhang & Meszaros 2002 the following relation should be satisfied:

$$E_p \propto L^{1/2}\Gamma^{-2} \quad (6)$$

where L is the luminosity and Γ is the bulk Lorentz factor of the shock. If the spectral shape does not change, the normalization constant K of Eq. 3 is proportional to the luminosity. As the α and β are not well constrained in the multi-component model due to the correlation of the parameters among the components, the luminosity is not well constrained. We have plotted the E_p-K relation in Figure 10. If Γ is constant and the spectral shape does not change during the emission, we expect that E_p will be proportional to $K^{1/2}$. No clear correlation is found for component A (filled circle). For component B_1 (filled triangle) the expected correlation is not found either, and it shows a negative correlation.

The higher energy components of the interval 2, C_1 and C_2, which correspond to the two peaks seen in the 40$\sim$80 keV light curve, are resolved as a broken power law spectrum for which E_p is around 50 $\sim$ 90 keV. If we assume that E_p decreases exponentially as seen in many GRBs, we can derive the correspondence among the E_p as indicated in Figure 8. The decay constant of the E_p is $\sim$20 sec.

At interval 3, the first precursor component seen in interval 1a (component A) is not well resolved. Component B_2 has a similar E_p to that of component B_1, but its E_p is somehow systematically higher than the extrapolation of B_1. Assuming that B_2 is thermal emission, its radiation radius is calculated and shown in Figure 9. The radiation radius is well below the extrapolation of those for B_1. The E_p-K relation of B_2 is shown in Figure 10, and it does not follow the relation given by Eq. 6.

The highly variable spectra whose emission peaks vary from 100 keV to 40 keV are also resolved (C_3, C_4), and they correspond to the emissions seen in the light curve of the highest energy band. From Figure 8, the E_p of the components decrease exponentially with time with a decay constant of $\sim$5 sec.

The E_p-K relations for components C_1, C_2, C_3 and C_4 are also shown in Figure 10. Although there are few data points for each component, the E_p-K relation is satisfied except for two points. Both the exceptions are at the time intervals corresponding to the rising part of the components C_1 and C_3. During the rise, due to the curvature effect, the emission from a part of the shock front that is moving toward us dominates. After that, the emission is averaged over a wider region, so the emission properties may change between the rising part and the following part.

In interval 4a, component B_2 is likely to remain and a black body spectrum with $T = 1$ keV or a broken power law spectrum with $E_p \sim 4$ keV is also likely to be present. In interval 4b, a power law spectrum with photon index 1.9 is the most preferred model, which is almost the same as the afterglow spectrum observed by Chandra.

5. Conclusion

We have analyzed the time resolved spectra of GRB 041006 and successfully resolved the components corresponding to the hard spikes and the soft broad bump observed in the multi-energy band light curves. The components may be divided into two classes. One is component A, which has almost constant E_p around 6 keV, and components B_1 and B_2 which have almost constant E_p around 20 keV. E_p for this class gradually decreases on a timescale, 60$\sim$70 s. The spectral type is well represented by a broken power law function or a black body radiation function. Assuming that the emission of this component is due to black body radiation, we derived the emission radii. At the beginning of the emission they are 4×10^6 km for component A and 7×10^5 km for components B_1 and B_2. The expansion velocity in the source frame is also derived; it is 0.78 c and 0.4 c for components A and B_1, respectively. The emission radius of component B_2 is almost constant.

The E_p-Luminosity relation is examined for these components and compared with the prediction of the internal shock model. We used a normalization constant K in Eq. 3 instead of deriving the luminosity. According to the internal shock model of Zhang & Meszaros 2002, E_p is proportional to $L^{1/2}$ if the bulk Lorentz factor of the shock is constant during the emission. We could not find such a correlation for components A, B_1 and B_2.

The second class comprises the components whose E_p is

larger than the former class and shows a relatively rapid decrease on a timescale of $5 \sim 20$ sec. The spectra are well represented by a broken power law function, and the E_p-K relation almost follows the relation expected for an internal shock origin, so this could explain their origin.

We could not reach a conclusion about the origin of the soft component observed for GRB 041006. However, the difference in its time variability with respect to the higher energy component suggests that it originates from different emission sites, such as acceleration by a wider jet, emission from a supernova shock breakout, or emission from the photosphere of the fireball.

Acknowledgements

We would like to thank the HETE-2 team members for their support. The HETE-2 mission is supported in the US by NASA contract NASW-4690; in Japan in part by Grant-in-Aid 14079102 from the Ministry of Education, Culture, Sports, Science, and Technology; and in France by CNES contract 793-01-8479. YS is grateful for support under the JSPS Core-to-Core Program, Grant-in-aid for Information Science (15017289 and 18049074) and Young Scientists (B) (17700085) carried out by the Ministry of Education, Culture, Sports, Science and Technology of Japan. KH is grateful for support under MIT Contract SC-A-293291,

energy range	T50(s)	T90(s)
2 – 10 keV	13.9±0.08	38.2±0.40
10 – 25 keV	11.9±0.16	27.3±1.44
40 – 80 keV	10.2±0.09	19.6±0.10
80 – 400 keV	3.7 ±0.25	17.4±0.25

Table 1. Temporal properties, T_{50} and T_{90}, of GRB 041006. The quoted errors correspond to one sigma.

time interval id	start (s) – end (s)
1a	2.5 – 6.0
1b	6.0 – 12.5
2a	12.5 – 16.5
2b	16.5 – 19.5
2c	19.5 – 23.0
2d	23.0 – 27.5
3a	27.5 – 29.5
3b	29.5 – 31.0
3c	31.0 – 34.0
3d	34.0 – 38.0
4a	38.0 – 42.5
4b	42.5 – 60.0
2a'	15.0 – 16.5
2c'	22.0 – 24.0
3b'	30.0 – 32.0
3c'	33.0 – 35.0

Table 2. Time intervals used for time resolved spectral analysis. The offset time is the trigger time 20041006_121808.63933.

model	n	k	χ^2	p	AIC	Δ_X (90% limit)	
bbody*2+bknp	83	8	74.35	0.499	6.87	–	T=1.4,5.5,Ep=74
bknp*3	83	12	68.84	0.551	8.47	1.6(4.7)	Ep=5,25,72
bbody+bknp*2	83	10	73.75	0.453	10.19	3.32(4.1)	T=1.6,Ep=23,73
bknp*2	83	8	77.80	0.390	10.63	3.76(<0)	Ep=5,24
band	83	4	96.55	0.087	20.55	13.68(<0)	Ep=38
bknp	83	4	111.19	0.010	32.27	25.40(<0)	Ep=22

Table 3. Results of the spectral fit to the time averaged spectrum. n is the number of data points used for the fit, k is the number of model parameters, χ^2 is the chi-square of the fit, p is the null hypothesis probability, AIC is the Akaike information criterion, and Δ_X is the AIC difference between the corresponding model and the lowest AIC model. The numbers in parentheses represent the 90% confidence limits of the AIC. The expected value of the fitting parameters are shown in the last column, where T is the black body temperature in keV and E_p is the break energy of the `brknp` model in keV.

model	component	parameters			
bbody*2+bknp	1	$kT = 1.40^{+0.22}_{-0.16}$	$K_{\rm bbody} = 0.16 \pm 0.04$		
	2	$kT = 5.53^{+0.77}_{-0.67}$	$K_{\rm bbody} = 0.44 \pm 0.10$		
	3	$E_p = 73.5^{+7.6}_{-15.6}$	$\alpha = 1.33^{+0.09}_{-0.14}$	$\beta = 2.96^{+1.19}_{-0.60}$	$K_{\rm bknp} = 37.8^{+6.2}_{-6.1}$
bknp*3	1	$E_p = 71.9^{+16}_{-9.6}$	$\alpha = 1.3^{+0.2}_{-3.3}$	$\beta = 2.9^{+1.2}_{-0.4}$	$K_{\rm bknp} = 43.4^{+3.5}_{-27}$
	2	$E_p = 25.4^{+2.0}_{-4.0}$	$\alpha = 1.2^{+0.3}_{-0.9}$	$\beta = 5.00^{+0.0}_{-2.5}$	$K_{\rm bknp} = 19.8^{+24}_{-3.3}$
	3	$E_p = 4.9^{+1.3}_{-0.6}$	$\alpha = -2.00^{+3.0}_{-0.0}$	$\beta = 2.9^{+2.1}_{-0.4}$	$K_{\rm bknp} = 3.69^{+5.2}_{-1.0}$

Table 4. Fitting parameters for the time averaged spectrum. kT and $K_{bbody} = R^2_{km}/D^2_{10}$ are the temperature and normalization constanat for the black-body radiation model, respectively. R_{km} is the source radius in km. D_{10} is the distance to the source in units of 10 kpc. E_p, α, β, K_{bknp} are the break energy, low energy photon index, high energy photon index, and normalization constant defined in Eq. 3. The unit of $K_{\rm bknp}$ is keV cm^{-2} s^{-1}.

Table 5. Results of spectral model fitting to the time resolved spectra. n is the number of data used for the fit, k is the number of model parameters, χ^2 is the chi-square of the fit, and p is the null hypothesis probability, AIC is the Akaike information criterion, Δ_X is the AIC difference between the corresponding model and the lowest AIC model. The numbers in parentheses represent the 90% confidence limit of the AIC. The expected value of the fitting parameters are shown in the last column, where T is the black body temperature in unit keV, E_p is the break energy of the `brknp` model measured in keV, a is the power law photon index of the `pl` model, and n_H is the column density measured in unit 10^{22}.

interval	model	n	k	χ^2	p	AIC	Δ_X(90%C.L.)	
1a	bbody	52	2	41.38	0.802	-7.87	–	T=2
	bknp	52	4	40.75	0.762	-4.68	3.19(3.9)	Ep=7.3
	wabs*pl	52	3	47.26	0.544	1.03	8.90(1.1)	a=3.0,nH=16
	pl	52	2	56.57	0.243	8.38	16.25(0.0)	a=2.1
1b	bbody*2	52	4	36.27	0.893	-10.73	–	T=1.4,5.9
	bbody+bknp	52	6	35.92	0.857	-7.24	3.49(4.2)	T=1.5,Ep=30
	bknp*2	52	8	35.60	0.813	-3.70	7.03(7.4)	Ep=6,30
	bknp	52	4	42.92	0.681	-1.98	8.75(<0)	Ep=6
	bbody+pl	52	4	49.93	0.396	5.89	16.62(<0)	T=2.1,a=1.9
	pl	52	2	63.52	0.095	14.41	25.14(<0)	p=1.9
2a	bbody*2+bknp	80	8	59.34	0.857	-7.90	–	T=1.7,5.9,Ep=84
	bknp*2	80	8	61.24	0.813	-5.38	2.52(4.1)	Ep=24,83
	bbody+bknp*2	80	10	58.43	0.837	-5.14	2.76(4.2)	T=2.6,Ep=23,83
	bknp*3	80	12	57.68	0.810	-2.17	5.73(9.4)	Ep=5,24,83
	bknp	80	4	70.48	0.657	-2.13	5.77(0.5)	Ep=25
2b	bbody*2+bknp	80	8	104.91	0.007	37.69	–	T=1.4,5.4,Ep=84
	bbody*2+bknp*2	80	12	99.33	0.008	41.31	3.77(6.2)	T=1.4,5.5,Ep=50,85
	bbody+bknp	80	6	116.18	0.001	41.85	3.99(2.0)	T=1.5,Ep=21
	bknp	80	4	122.30	0.001	41.96	4.10(1.7)	Ep=23
	bknp*2	80	8	111.59	0.002	42.63	4.77(4.1)	Ep=23,85
	bknp*3	80	12	101.08	0.006	42.71	4.78(8.2)	Ep=5,22,85
	bbody+bknp*2	80	10	106.05	0.004	42.55	5.22(5.5)	T=1.5,Ep=22,85
2c	bbody*2+bknp*2	73	12	49.53	0.853	-4.32	–	T=1.3,5.0,Ep=52,98
	bbody*2+bknp	73	8	56.66	0.760	-2.50	1.67(<0)	T=1.3,5.0,Ep=53
	bbody+bknp*2	73	10	56.61	0.702	1.44	5.76(0.2)	T=1.5,Ep=18,54
	bknp*3	73	12	53.58	0.739	1.42	5.74(0.2)	Ep=5.5,18,74
	bknp*2	73	8	62.24	0.574	4.36	8.68(0.06)	Ep=19,54
	bbody+bknp	73	6	66.70	0.488	5.41	9.73(<0)	T=4.7,Ep=55
	bknp	73	4	87.99	0.006	21.63	25.72(<0)	Ep=23
2d	bbody*2+bknp	66	8	64.70	0.254	14.69	—-	T=1.2,4.6,Ep=62
	bbody+bknp	66	6	72.12	0.136	17.85	3.16(0.9)	T=4.5,Ep=62
	bknp*2	66	8	70.33	0.129	20.19	5.50(1.2)	Ep=18,59
	bknp	66	4	80.21	0.060	20.87	6.18(0.1)	Ep=18
	bbody+bknp*2	66	10	67.50	0.140	21.48	6.79(5.5)	T=1.6,Ep=17,60
	bknp*3	66	12	66.84	0.113	24.83	10.14(4.4)	Ep=4,17,60
3a	bbody+bknp	74	6	63.37	0.636	0.53	–	T=6.8,Ep=96
	bknp*2	74	8	63.72	0.557	4.93	4.40(4.9)	Ep=27,95
	bbody+bknp*2	74	10	61.83	0.554	6.71	6.18(6.8)	T=6.0,Ep=50,92
	bknp	74	4	75.48	0.306	9.46	8.93(3.4)	Ep=36
	bknp*3	74	12	62.21	0.469	11.15	10.62(11.8)	Ep=26,45,96
3b	bknp*2	84	8	80.20	0.349	12.11	–	Ep=25,82
	bknp*2+pl	84	10	79.57	0.308	15.45	3.34(3.9)	Ep=26,84,a=1.3
	bbody+bknp+pl	84	8	83.64	0.257	15.64	3.53(3.0)	T=8,Ep=84,a=1.6
	bknp*4	84	16	69.19	0.437	15.69	3.58(8.6)	Ep=6,10,21,84
	bbody+bknp*2	84	10	80.17	0.292	16.08	3.97(4.0)	T=0.9,Ep=26,80
	bbody+bknp	84	6	85.91	0.413	17.89	5.78(<0)	T=8,Ep=83
	bknp*3	84	12	79.88	0.245	19.78	7.67(7.2)	Ep=5,26,80
	bknp	84	4	107.35	0.022	28.60	16.49(<0)	Ep=67
3c	bknp*3	73	12	70.36	0.193	21.32	–	Ep=26,44,120
	bbody+bknp*3	73	14	67.43	0.211	22.20	0.88(4.5)	T=1.2,Ep=26,44,118
	bknp*2	73	8	80.75	0.090	23.37	2.05(2.3)	Ep=44,130
	bbody+bknp*2	73	10	78.07	0.096	24.90	3.58(1.3)	T=1.1,Ep=44,117

Table 5. (Continued.)

interval	model	n	k	χ^2	p	AIC	Δ_X(90%C.L.)	
	bknp*4	73	16	67.91	0.153	26.72	5.40(7.4)	Ep=6,26,44,119
	bknp	73	4	98.92	0.011	30.18	8.86(<0)	Ep=56
3d	bbody+bknp	80	6	76.28	0.405	8.19	–	T=6.1,Ep=72
	bknp*2	80	8	77.40	0.310	13.36	5.17(5.8)	Ep=21,47
	bknp	80	4	86.42	0.194	14.18	5.99(<0)	Ep=24
	bknp*3	80	12	74.91	0.264	18.74	10.55(13.6)	Ep=23,43,75
4a	bbody*2	66	4	59.23	0.576	0.86		T=1.2,5.2
	bbody+bknp	66	6	59.14	0.505	4.76	3.90(7.1)	T=1.2,Ep=24
	bknp	66	4	63.09	0.438	5.02	4.16(2.8)	Ep=26
	bknp*2	66	8	57.36	0.496	6.74	5.88(7.4)	Ep=4,25
	bbody+pl	66	4	73.06	0.159	14.71	13.85(1.4)	T=4.7,a=2.3
	pl	66	2	100.05	0.003	31.46	30.60(<0)	a=2.0
4b	pl	52	2	47.31	0.582	-0.92	–	a=1.9
	bbody+pl	52	4	44.82	0.604	0.27	1.19(3.1)	T=1.5,a=1.8
	bknp	52	4	45.13	0.591	0.63	1.55(3.6)	Ep=4
	bbody	52	2	69.71	0.034	19.24	20.16(0.0)	T=1.7

interval	component	parameters			
1a	1	$kT = 1.92^{+0.30}_{-0.27}$	$K_{\rm bbody} = 9.94^{+0.71}_{-0.42} \times 10^1$		
1b	1	$kT = 1.44^{+0.18}_{-0.17}$	$K_{\rm bbody} = 4.17^{+2.2}_{-1.4} \times 10^2$		
	2	$kT = 5.94^{+1.26}_{-1.08}$	$K_{\rm bbody} = 1.89^{+2.1}_{-0.99}$		
2a	1	$kT = 1.60^{+0.84}_{-0.21}$	$K_{\rm bbody} = 2.38^{+7.1}_{-2.3} \times 10^2$		
	2	$kT = 5.75^{+1.4}_{-1.2}$	$K_{\rm bbody} = 3.95^{+5.9}_{-3.3}$		
	3	$E_p = 83.2^{+15.2}_{-10.6}$	$\alpha = 1.45^{+0.20}_{-0.41}$	$\beta = 5.00^{+0.0}_{-1.8}$	$K_{\rm bknp} = 48.9^{+5.8}_{-11}$
2b	1	$kT = 1.40^{+0.23}_{-0.17}$	$K_{\rm bbody} = 1.02^{+0.73}_{-0.63} \times 10^3$		
	2	$kT = 5.40^{+0.59}_{-0.49}$	$K_{\rm bbody} = 13.0^{+6.7}_{-5.7}$		
	3	$E_p = 84.3^{+8.4}_{-32}$	$\alpha = 1.26^{+0.46}_{-0.83}$	$\beta = 5.00^{+0.00}_{-0.94}$	$K_{\rm bknp} = 57.8^{+13.9}_{-12.2}$
2c	1	$kT = 1.34^{+0.18}_{-0.077}$	$K_{\rm bbody} = 1.44^{+0.56}_{-0.43} \times 10^3$		
	2	$kT = 5.01^{+1.1}_{-0.46}$	$K_{\rm bbody} = 25.0^{+6.9}_{-13}$		
	3	$E_p = 52.3^{+5.0}_{-7.6}$	$\alpha = 0.24^{+1.0}_{-2.2}$	$\beta = 5.00^{+0.0}_{-1.9}$	$K_{\rm bknp} = 97.9^{+35}_{-40}$
	4	$E_p = 95.5^{+13.0}_{-9.7}$	$\alpha = 0.06^{+1.4}_{-2.1}$	$\beta = 5.00^{+0.00}_{-1.4}$	$K_{\rm bknp} = 78.4^{+19}_{-50}$
2d	1	$kT = 1.28^{+0.47}_{-0.19}$	$K_{\rm bbody} = 1.01^{+0.95}_{-0.85} \times 10^3$		
	2	$kT = 4.65^{+0.42}_{-0.33}$	$K_{\rm bbody} = 26.3^{+9.7}_{-9.4}$		
	3	$E_p = 62.1^{+7.1}_{-11.5}$	$\alpha = 1.22^{+0.3}_{-1.1}$	$\beta = 5.00^{+0.0}_{-1.4}$	$K_{\rm bknp} = 54.1^{+11.5}_{-10.9}$
3a	1	$kT = 6.8^{+1.2}_{-1.1}$	$K_{\rm bbody} = 3.61^{+2.9}_{-1.5}$		
	2	$E_p = 95.8^{+8.5}_{-15}$	$\alpha = 1.50^{+0.07}_{-0.07}$	$\beta = 5.00^{+0.0}_{-1.5}$	$K_{\rm bknp} = 107^{+17}_{-18}$
3b	1	$E_p = 25.3^{+3.5}_{-2.6}$	$\alpha = -0.92^{+1.5}_{-1.1}$	$\beta = 5.00^{+0.0}_{-3.2}$	$K = 68.7^{+11}_{-11}$
	2	$E_p = 81.9^{+7.3}_{-9.9}$	$\alpha = 1.05^{+0.15}_{-0.10}$	$\beta = 3.28^{+0.52}_{-0.46}$	$K = 386^{+32}_{-71}$
3c	1	$E_p = 25.8^{+2.4}_{-4.0}$	$\alpha = -0.10^{+0.72}_{-1.9}$	$\beta = 5.00^{+0.0}_{-2.8}$	$K = 68.1^{+15}_{-45}$
	2	$E_p = 44.0^{+13}_{-3.6}$	$\alpha = -2.00^{+2.7}_{-0.00}$	$\beta = 2.66^{+2.0}_{-0.39}$	$K = 115^{+30}_{-62}$
	3	$E_p = 119^{+11}_{-12}$	$\alpha = 1.33^{+0.05}_{-0.11}$	$\beta = 5.00^{+0.00}_{-1.40}$	$K = 159^{+95}_{-48}$
3d	1	$kT = 6.05^{+0.71}_{-0.69}$	$K_{\rm bbody} = 5.18^{+2.4}_{-1.6}$		
	2	$E_p = 71.9^{+14}_{-30}$	$\alpha = 1.39^{+0.05}_{-0.10}$	$\beta = 4.32^{+0.68}_{-1.5}$	$K = 55.7^{+12}_{-12}$
4a	1	$kT = 1.23^{+0.18}_{-0.16}$	$K_{\rm bbody} = 8.09^{+5.6}_{-3.1} \times 10^2$		
	2	$kT = 5.16^{+0.81}_{-0.71}$	$K_{\rm bbody} = 4.66^{+3.5}_{-2.0}$		
4b	1	$\alpha = 1.93^{+0.16}_{-0.14}$	$K_{\rm pl} = 2.74^{+0.90}_{-0.68}$		

Table 6. Fitting parameters for the most preferred models, that is, the model that gives the lowest AIC. kT and $K_{\rm bbody} = R^2_{km}/D^2_{10}$ are the temperature and normalization constant for the black-body radiation model, respectively. R_{km} is the source radius in km. D_{10} is the distance to the source in units of 10 kpc. E_p, α, β, $K_{\rm bknp}$ are the break energy, low energy photon index, high energy photon index, and normalization constant defined in Eq. 3. The unit of $K_{\rm bknp}$ is keV cm^{-2} s^{-1}. K_{pl} is the normalization constant for power law spectrum defined as photon flux at 1 keV in unit of photons keV^{-1} cm^{-2} s^{-1}.

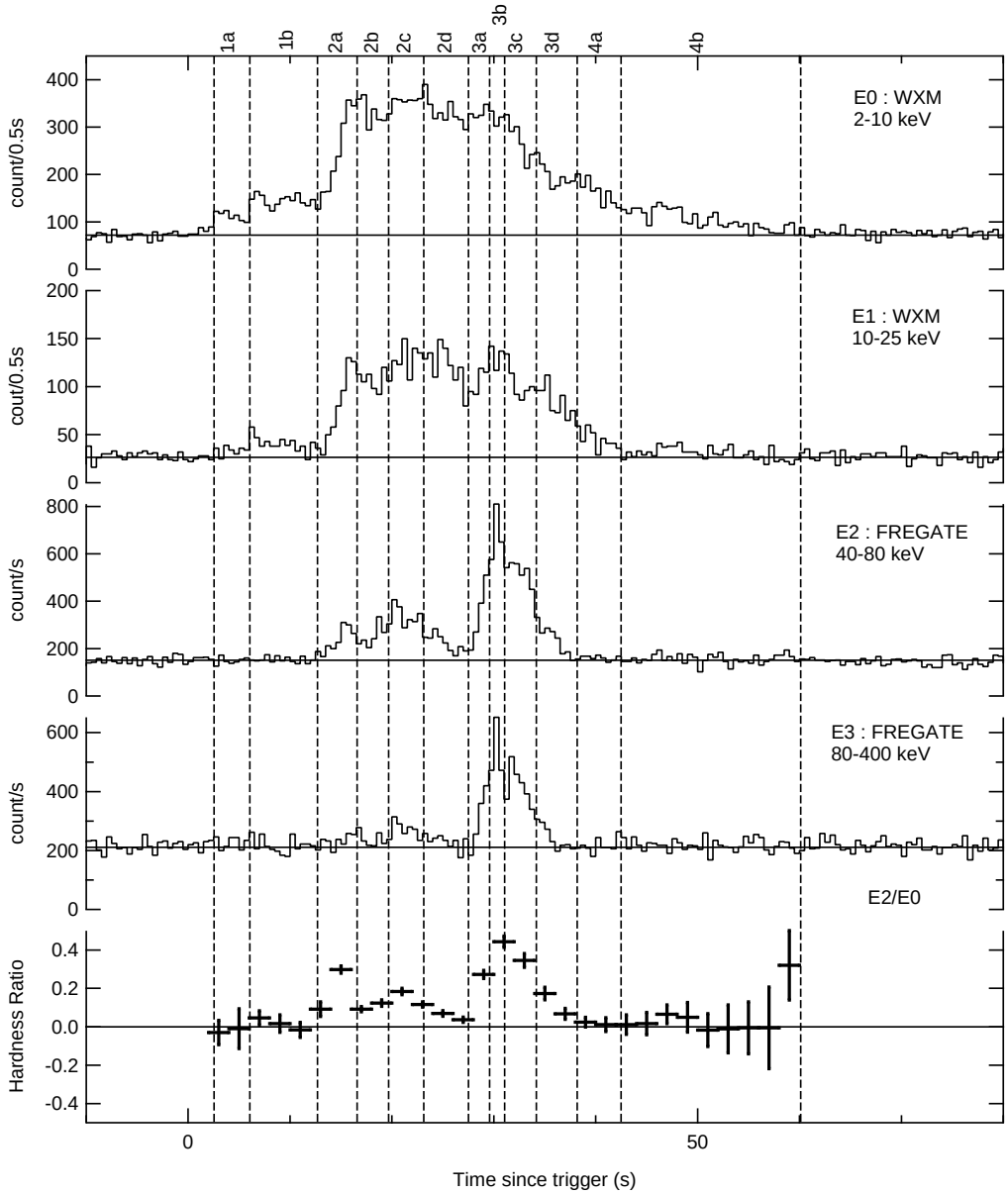

Fig. 1. Light curves of GRB041006 for four energy bands and hardness ratio. From top to bottom, 2–10 keV, 10–25 keV, 40–80 keV, and 80–400 keV. The hardness ratio is calculated by dividing the 40∼80 keV count rate by the 2∼10 keV count rate. The vertical lines represent the boundaries of the time intervals for time resolved spectral analysis.

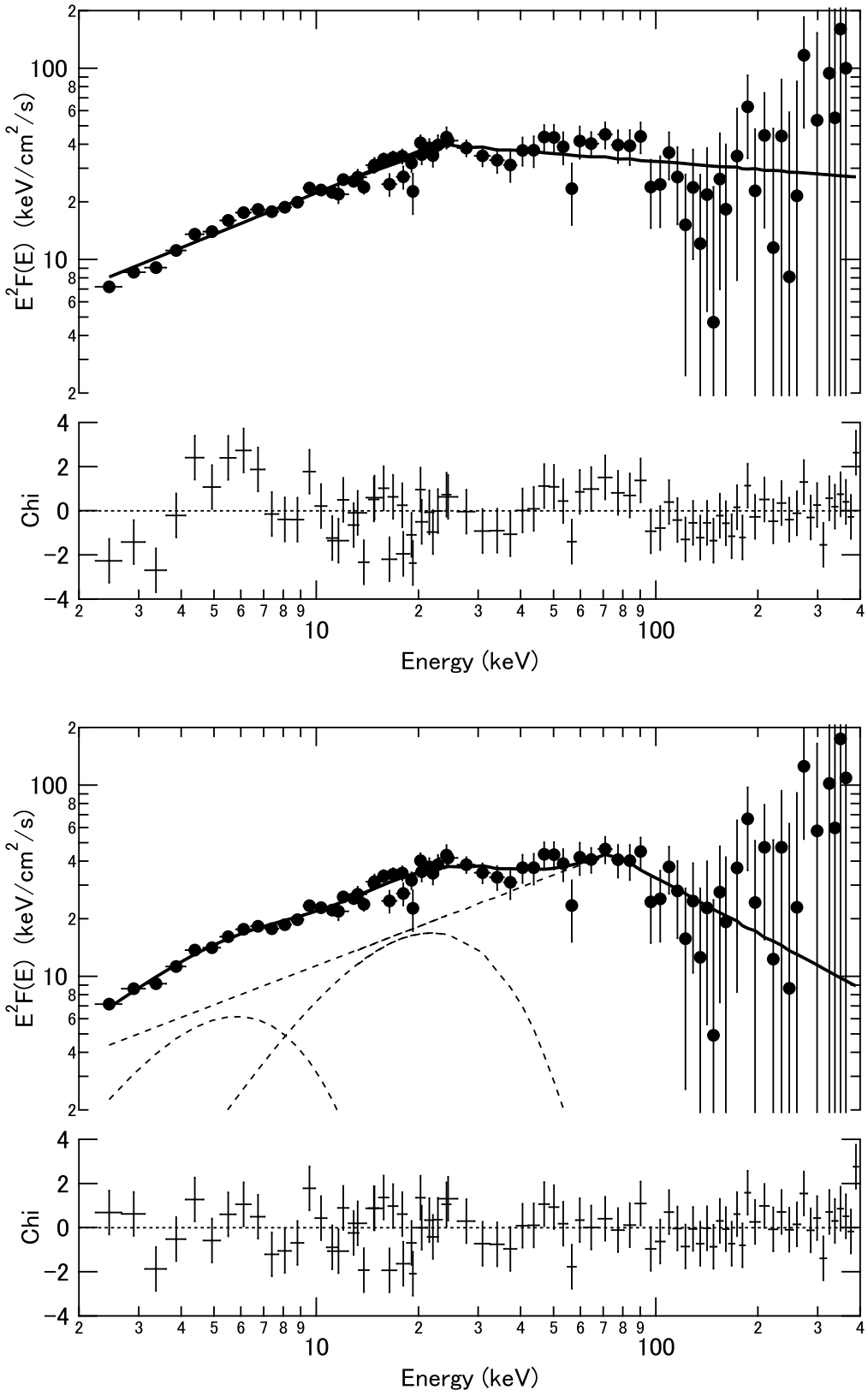

Fig. 2. Time averaged unfolded spectrum expressed in νf_ν. Top: Fitting result for the broken power law model. Bottom: Fitting result for the three-component model represented by a superposition of three broken power law functions.

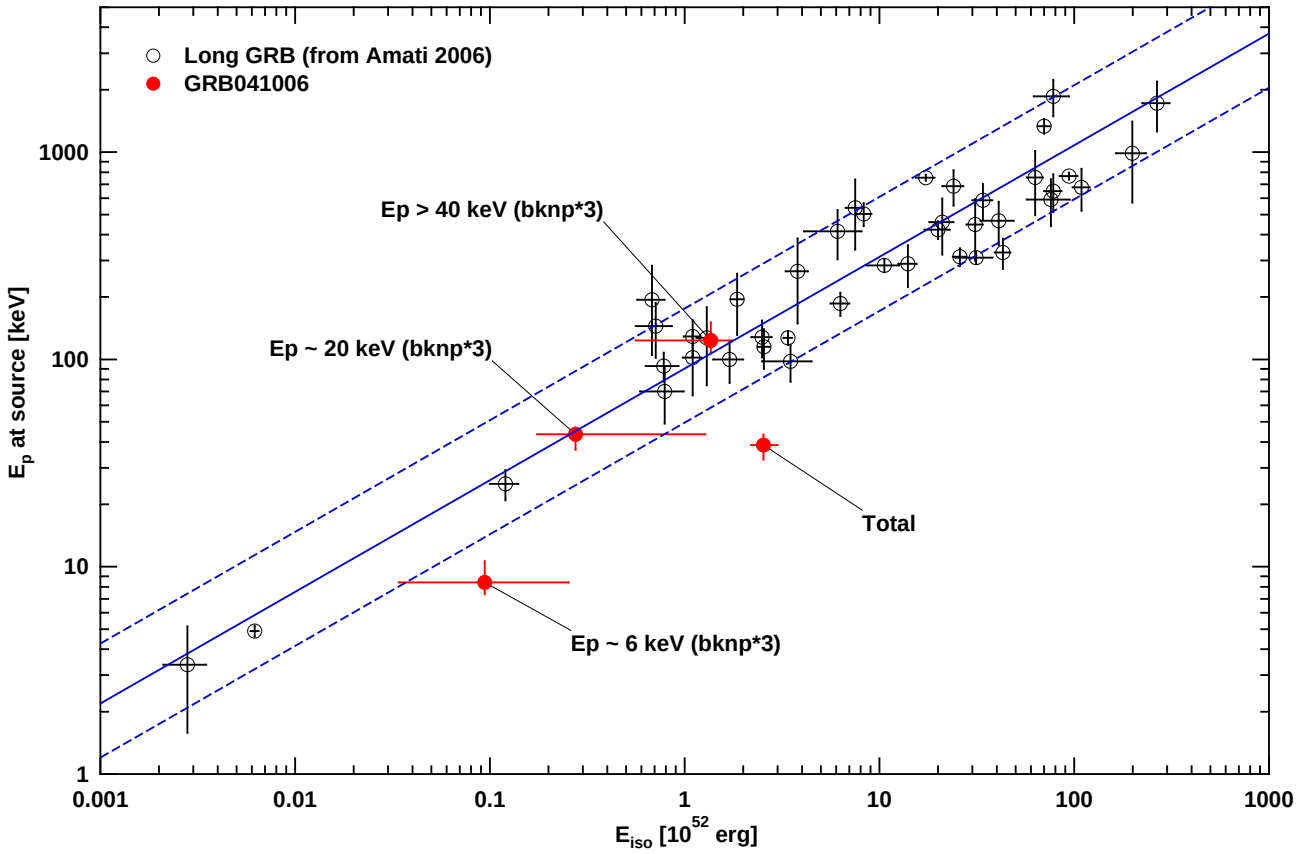

Fig. 3. $E_{\rm p,src}$-$E_{\rm iso}$ relation for long GRBs. The open circles represent the long GRBs compiled by Amati 2006. The solid circles represent GRB 041006. The solid circle labeled "Total" is derived from a single broken power model. The other solid circles are derived from a `bknp*3` model. The solid line represent the average relation derived from all the points of the open circles, while the dashed lines represent lower and upper boundaries which are parallel to the average relation and contain 90% of the points.

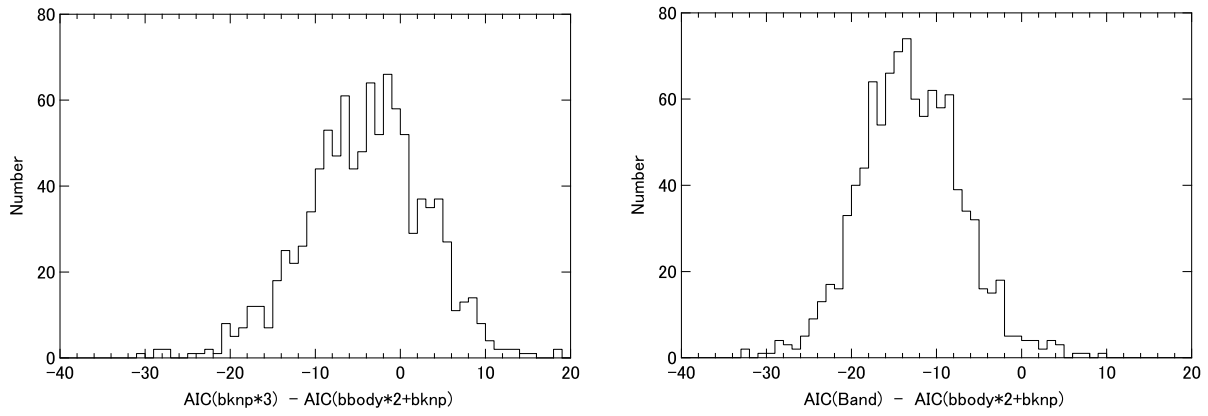

Fig. 4. Left: Simulated distribution of AIC differences between the `bknp*3` and `bbody*2+bknp` models (left). The simulation is performed using the `bknp*3` model, and model fitting to the simulated data is carried out for both the models. The `bbody*2+bknp` model is the most preferable model for the time integrated spectrum. The AICs for the two model are calculated for each simulated spectrum. The fraction of events with $\Delta_{AIC} > 0$ corresponds to the probability of selecting the wrong model. Right: Same plot for the Band model.

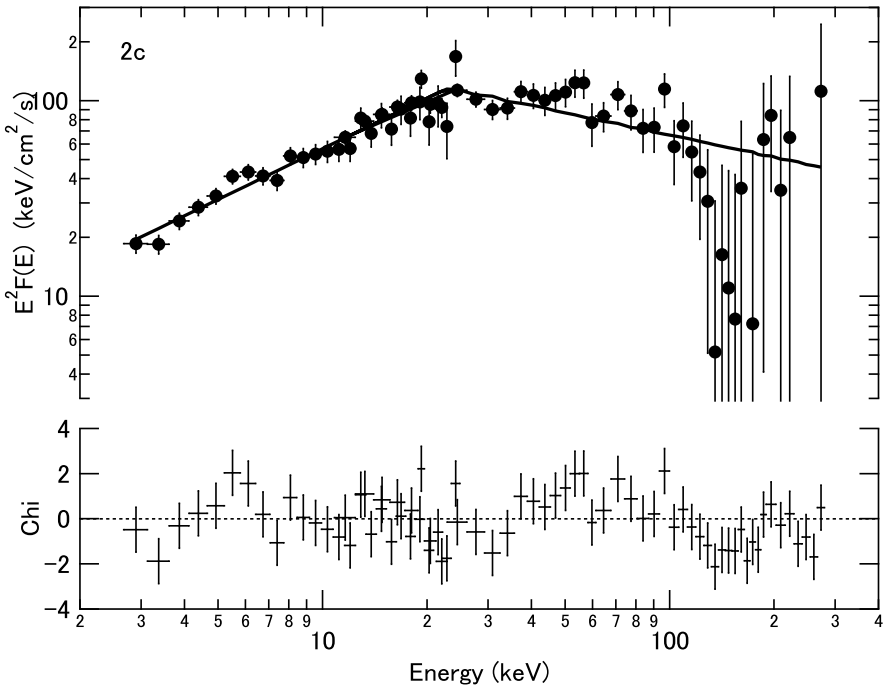

Fig. 5. An example of spectral fitting for interval 2c, where a single-component model is used.

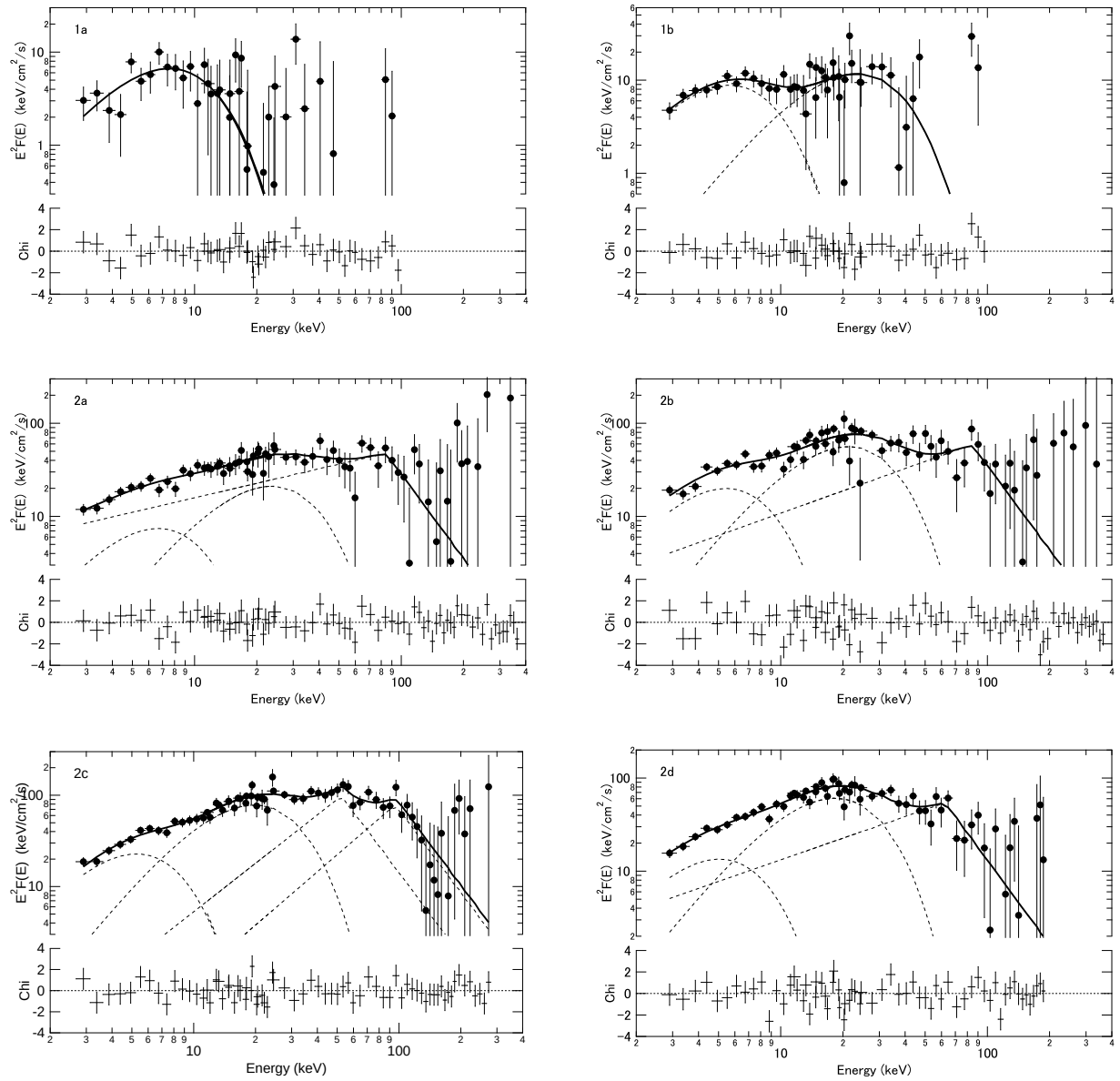

Fig. 6. Time resolved unfolded spectra for intervals 1 and 2. The residual between the observation and the model is also shown at the bottom panel of each figure. The spectrum is expressed in νf_ν. The most preferable model spectra are plotted as a solid line (total) and dashed lines (basic function).

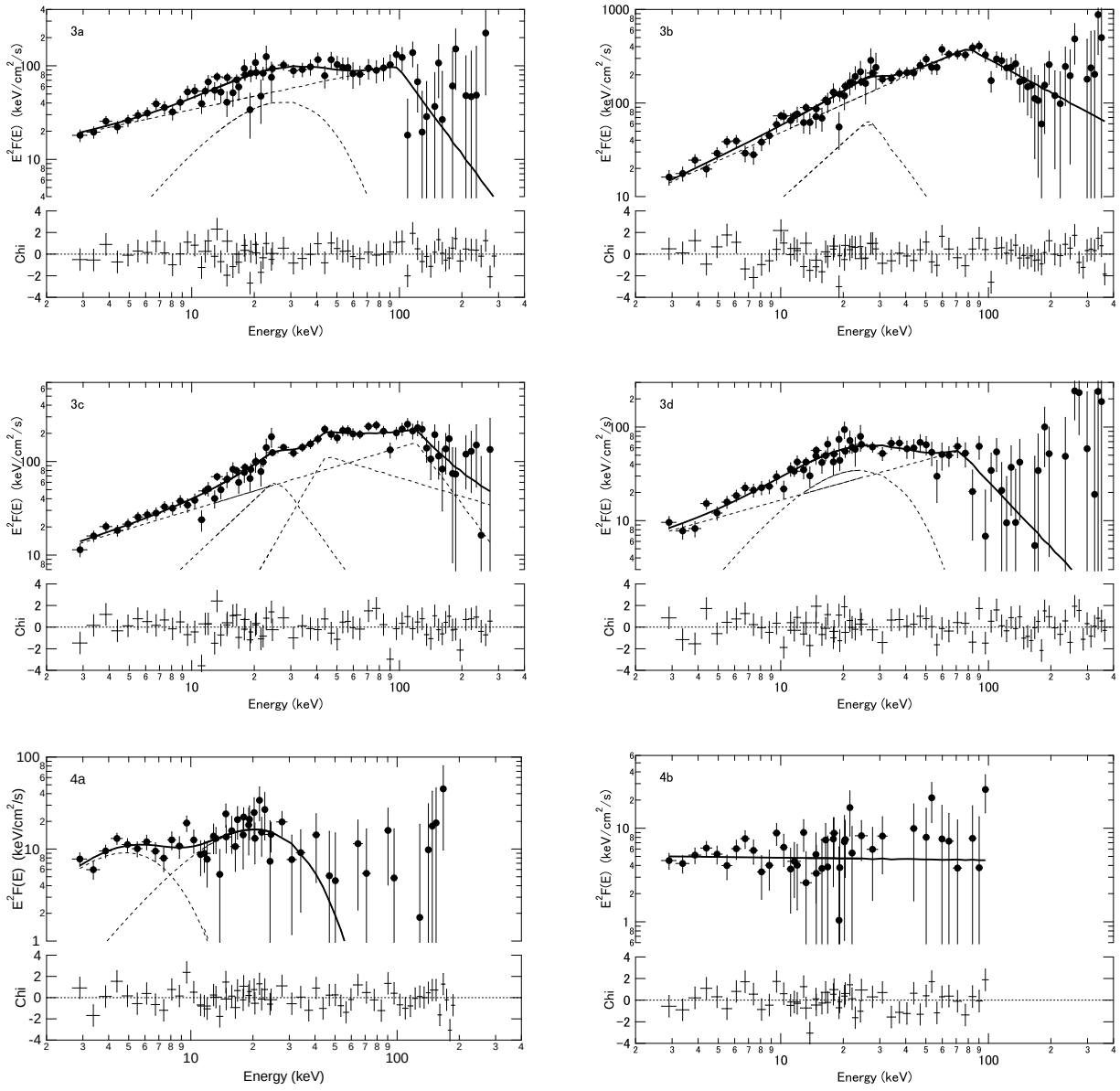

Fig. 7. Time resolved unfolded spectra for interval 3 and 4.

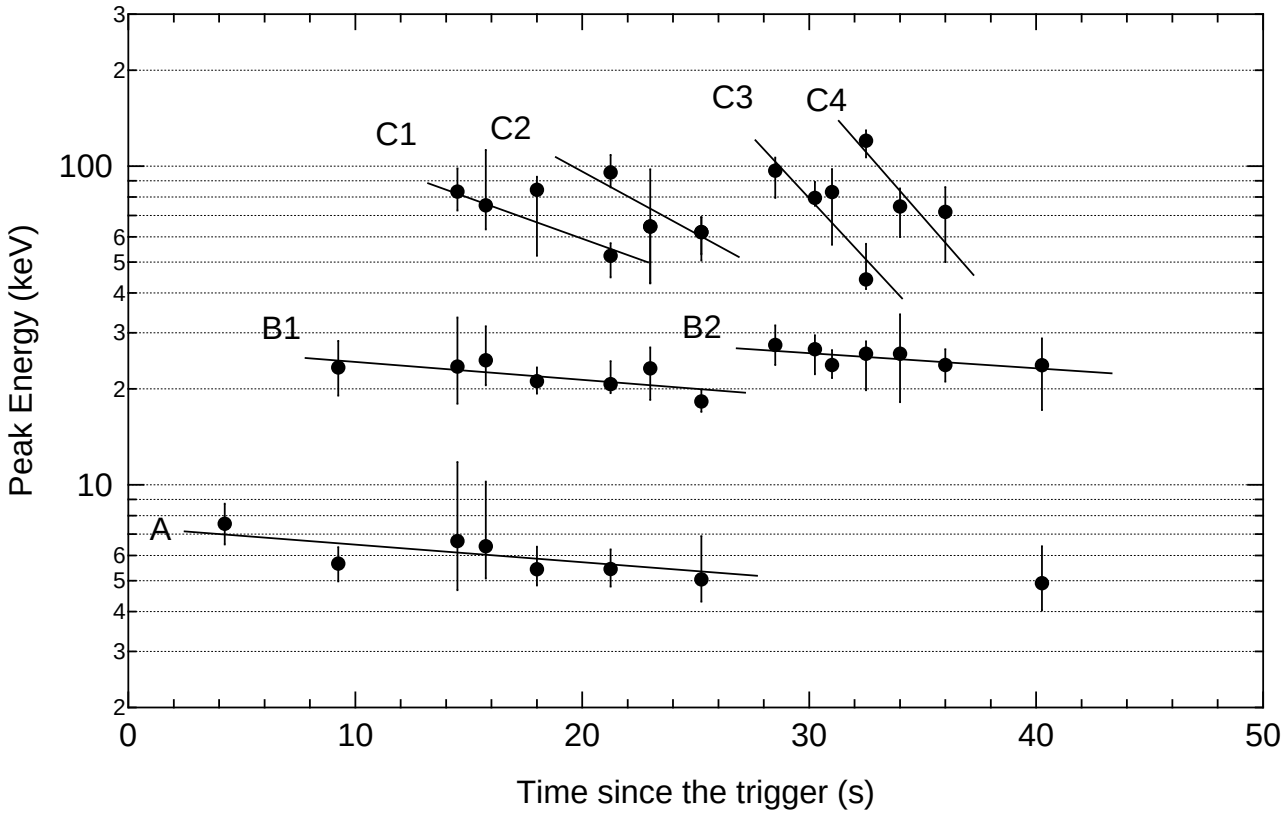

Fig. 8. Peak energy calculated for each interval by fitting the data with multi-component models. The points which are inferred to belong to identical components are interpolated with a line. The vertical error bar corresponds to 90% C.L.

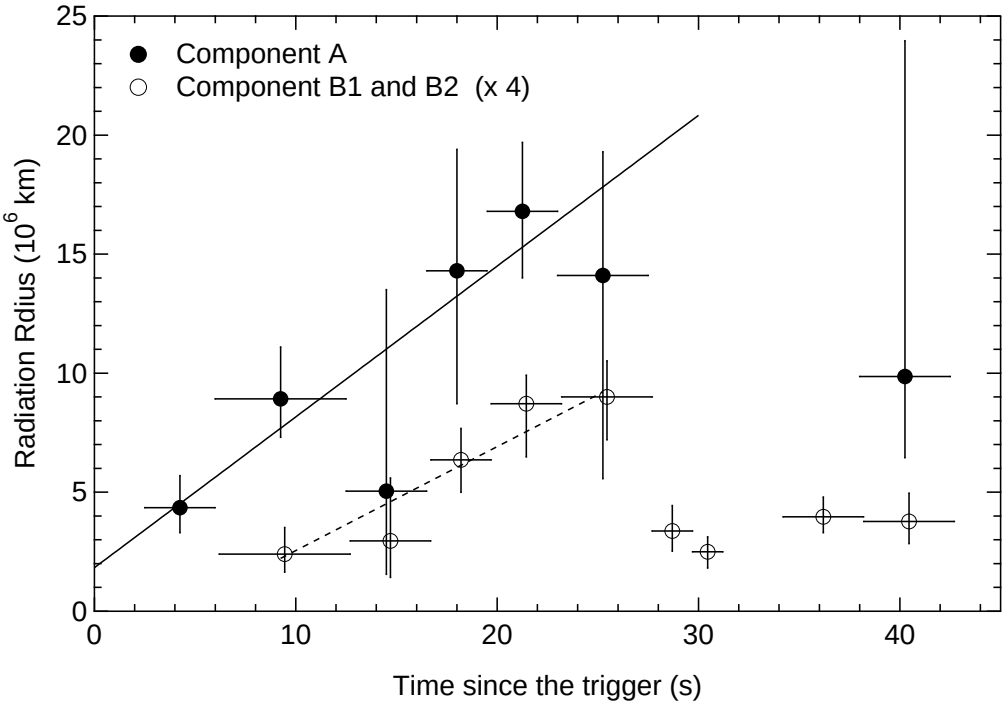

Fig. 9. Evolution of the radiation radii the black body components. The filled circles represent component A of Figure 8. The open circles represent components B_1 and B_2, for which the radius is multiplied by four. The solid and dashed lines represent the linear fit to the data of intervals 1 and 2.

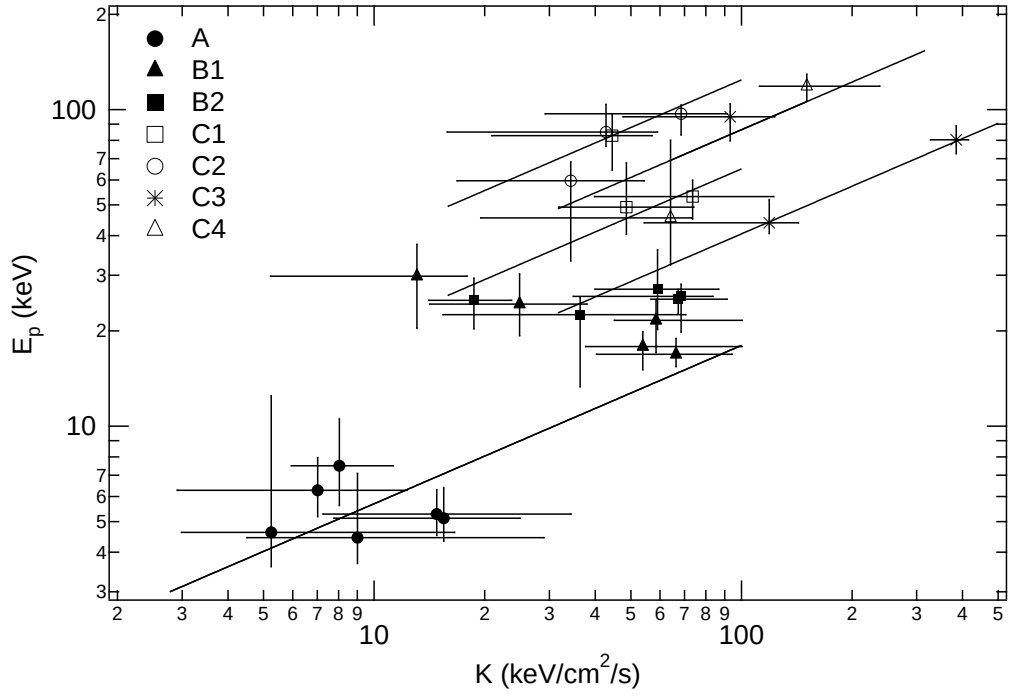

Fig. 10. The relation between E_p and K of Eq. 3 for each component. Solid lines represent the relation $E_p \propto K^{0.5}$.

References

Akaike, H. 1974, IEEE Transactions on Automatic Control **19**, 716

Amati, L. 2006, MNRAS, **372**, 233

Arnaud, K. A. 1996, in ASP Conf. Ser. 101: Astronomical Data Analysis Software and Systems V, ed. Jacoby, G. H. & Barnes, J., 17

Atteia, J.-L. et al. 2003, in Gamma-Ray Burst and Afterglow Astronomy, ed. Ricker, G. R. & Vanderspek, R. (Melville: AIP), 662, 17

Band, D. et al. 1993, ApJ, **413**, 281

Bikmaev, I. et al. 2004, GCN notice #2826

Borgonovo, L., Frontera, F., Guidorzi, C., Montanari, E., Vetere, L., and Soffitta, P. 2007, A&A, **465**, 765

Butler, N. R., Ricker, G. R., Ford, P. G., Vanderspek, R. K., Marshall, H. L., Jernigan, J. G., Garmire, G. P., & Lamb, D. Q. 2005, ApJ, **629**, 908

Cenko, S. B. et al. 2006, ApJ, **652**, 490

Chevalier, R. A. & Li, Zhi-Yun 2000, ApJ, **536**, 195

Da Costa, G. S. , Noel, N. & Price, P. A. 2004, GCN notice #2765

Daigne, F., & Mochkovitch, R. 2002, MNRAS, **336**, 1271

Fugazza, D. et al. 2004, GCN notice #2782

Galassi, M. et al 2004, GCN notice #2770

Garg, A. et al. 2004, GCN notice #2829

Ghirlanda, G., Nava, L., Ghisellini, G., & Firmani, C. 2007, A&A, **466**, 127

Granot, J. , Ramirez-Ruiz, E. & Perna, R. 2005, ApJ, 630, 1003.

Lazzati, D. 2005, MNRAS, **357**, 722

Murakami, T., Inoue, H., Nishimura, J., van Paradijs, J., & Fenimore, E. E. 1991, Nature, **350**, 592

Nava, L. , Ghisellini, G., Ghirlanda, G., Tavecchio, F., & Firmani, C. 2006, A&A, **450**, 471

Page, K. L. et al. 2007, ApJ, **663** 1125

Paczynsky, B. 1986, ApJ, **308**, L43

Piro, L. et al. 2005, ApJ, **623**, 314

Price, P. A. et al. 2004, GCN notice #2791

Ramirez-Ruiz, E., MacFadyen, A. I., & Lazzati, D. 2002, MNRAS, **331**, 197

Romano, P. et al. 2006, A&A, **456**, 917

Sakamoto, T. et al. 2005, ApJ, **629**, 311

Sari, R. , Piran, T. & Halpern, J. P. 1999, ApJ, **519**, L17

Shirasaki, Y. et al. 2003, PASJ, **55**, 1033

Soderberg, A. M. et al. 2004, GCN notice #2787

Soderberg, A. M. et al. 2006, ApJ, **636**, 391

Stanek, K. Z. et al. 2005, ApJ, **626**, L5

Umeda, H., Tominaga, N., Maeda, K., Nomoto, K. 2005, ApJ, **633** L17

Urata, Y. et al. 2007 ApJ, **655**, L81

Vanderspek, R. et al. 2004, ApJ, **617**, 1251

Vetere, L., Massaro, E., Costa, E., Soffitta, P., & Ventura, G. 2006, A&A, **447**, 499

Waxman, E. & Meszaros, P. 2003, ApJ, **584**, 390

Zhang, B., & Meszaros, P. 2002, ApJ, **581**, 1236